

# Beyond the blur: using experimentally determined point spread functions to improve scanning Kelvin probe imaging

Isaac C.D. Lenton\*,<sup>1</sup> Felix Pertl,<sup>1</sup> Lubuna Shafeek,<sup>1</sup> and Scott R. Waitukaitis<sup>1</sup>

<sup>1</sup>*Institute of Science and Technology Austria, Am Campus 1, 3400 Klosterneuburg, Austria*

(\*Electronic mail: isaac.lenton@ist.ac.at)

(Dated: 26 July 2024)

Scanning Kelvin probe microscopy (SKPM) is a powerful technique for investigating the electrostatic properties of material surfaces, enabling the imaging of variations in work function, topology, surface charge density, or combinations thereof. Regardless of the underlying signal source, SKPM results in a voltage image which is spatially distorted due to the finite size of the probe, long-range electrostatic interactions, mechanical and electrical noise, and the finite response time of the electronics. In order to recover the underlying signal, it is necessary to deconvolve the measurement with an appropriate point spread function (PSF) that accounts the aforementioned distortions, but determining this PSF is difficult. Here we describe how such PSFs can be determined experimentally, and show how they can be used to recover the underlying information of interest. We first consider the physical principles that enable SKPM, and discuss how these affect the system PSF. We then show how one can experimentally measure PSFs by looking at well defined features, and that these compare well to simulated PSFs, provided scans are performed extremely slowly and carefully. Next, we work at realistic scan speeds, and show that the idealised PSFs fail to capture temporal distortions in the scan direction. While simulating PSFs for these situations would be quite challenging, we show that measuring PSFs with similar scan conditions works well. Our approach clarifies the basic principles of and inherent challenges to SKPM measurements, and gives practical methods to improve results.

**Pre-print of:** J. Appl. Phys. 136, 045305 (2024) <https://doi.org/10.1063/5.0215151>

Copyright © 2024. This manuscript version is made available under the CC-BY-NC-ND 4.0

license <http://creativecommons.org/licenses/by-nc-nd/4.0/>.

## I. INTRODUCTION

SKPM enables imaging of the “invisible” electrostatic properties of surfaces at the mesoscale (typically  $>100\ \mu\text{m}$ ). By scanning a vibrating conductive probe above a surface and measuring/regulating the current induced within it (Fig. 1a), SKPM extracts information connected to the local electric potential<sup>1,2</sup>. This gives insight into various processes such as variations in work function or surface chemistry<sup>3,4</sup>, charge<sup>5,6</sup>, biological double layers<sup>7,8</sup>, *etc.* Though not identical, the operating principle behind SKPM is related to Kelvin probe force microscopy (KPFM)<sup>9</sup>, where measurement/regulation of the forces acting on a vibrating atomic force microscope tip permits similar imaging at the nanoscale<sup>10–12</sup>. One major advantage of SKPM over KPFM is the use of significantly larger probes enabling rapid scans over significantly larger areas (a discussion on the differences/similarities between the two techniques is included in the Supplementary Material, SM).

A fundamental problem in both SKPM and KPFM is properly interpreting and analyzing the measured signal. Regardless of the signal source (*e.g.* work function variations or charge), both techniques produce voltage images. Moreover, these images are spatially distorted due to the finite size of the probe, long-range electrostatic interactions<sup>13,14</sup>, mechanical and electrical noise<sup>15</sup>, and the temporal response of the electronics<sup>2,16,17</sup>. When these distortions are deterministic and linear, they can be characterised by a PSF, which describes the image an infinitesimally small point in the absence of noise would produce when measured. Effectively,

the measured signal is the convolution of the underlying signal with the PSF, and the underlying signal can be recovered by deconvolution<sup>13,14</sup>. Therefore, a key component in interpreting/analyzing SKPM (or KPFM) data relies on being able to determine the PSF that characterises the measurement process.

Toward addressing the problem, one can draw inspiration from optical microscopy. Like SKPM, optical images suffer from distortions, due to diffraction, optical imperfections, finite pixel sizes *etc.* To correct for these, a practical solution is to image the pattern created by a point-like emitter, *e.g.* a small fluorescent particle<sup>18</sup>. When this target is significantly smaller than the system resolution, the image rendered is approximately the PSF.

Here, we show that the approach of experimentally measuring PSFs is not only viable, but effective and straightforwardly implemented in the case of SKPM. Compared to KPFM, the larger probes used in SKPM allow scanning significantly larger areas at higher scan rates. Consequently, for SKPM it is possible to experimentally measure the PSFs using relatively large calibration targets. We restrict ourselves to the situation where the underlying signal is due to differences in material work functions on a planar surface, though in principle our ideas can be extended to other situations (*e.g.* variations in surface charge). We use common clean-room techniques to pattern regions with work function differences, which we image to extract PSFs. We find that when utilizing high scan speeds—which are necessary to probe large and/or time dependent features—the measured PSFs can differ significantly from those that only account for the electrostatic interactions between the probe and sample. We show

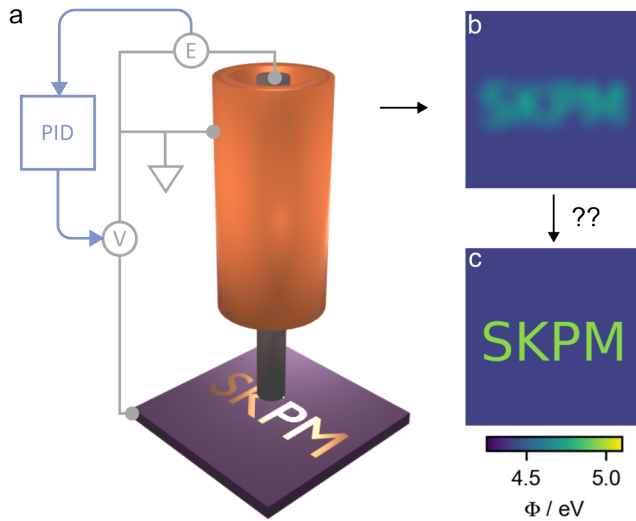


FIG. 1. **Principle of scanning Kelvin probe microscopy (SKPM).** **a** SKPM entails scanning a conductive probe above a sample to estimate the local surface potential. The cylindrical metal probe is vibrated vertically, while a lock-in amplifier and PID use feedback adjust the backing potential,  $V$ , so that the current in the probe is minimised. **b** Voltage maps measured by SKPM are spatially distorted, due to the probe's finite size, long-range electrostatics, and the temporal response of the electronics. **c** This paper is about extracting the true underlying surface potential from the measured signal, which we show is achievable by experimentally measuring the system's PSF and using this to deconvolve raw measurements.

that this is due to incorporation of temporal information into the PSF—an issue that would be difficult to account for analytically/computationally, but that is solved relatively easily in experiment. By simply measuring the PSF, we gain insight into the effect of measurement speed, feedback parameters, and probe geometry that would be difficult to predict or characterise independently. Our results outline a practical and easily implemented approach toward getting quantitative information out of SKPM.

## II. MEASUREMENT PRINCIPAL

### A. Signal acquisition

Figure 1a depicts an SKPM probe positioned above a sample and the feedback system used to acquire an estimate for the spatially varying surface potential of interest,  $V_S \equiv V_S(x)$ . The probe vibrates vertically at a fixed amplitude and frequency, while a potential ( $V$ ) is applied to the electrode at or below the sample. The current drawn to the probe due to the vibration is measured by an electrometer ( $E$ ) and further amplified by a lock-in amplifier which extracts the current signal due to the probe vibration and rejects noise at other frequencies. The signal acquired by SKPM is the value of the voltage,  $V$ , required to minimise the current induced in the probe as it is vibrated. This is typically accomplished by using feedback on the lock-in signal, *e.g.*, sending it to proportional-integral-

differential (PID) electronics and adjusting  $V$  until the current amplitude is zero. In the naïve version of the analysis, the probe-sample system is assumed to form a capacitor, where the image charge drawn to the probe is given by

$$Q(t) = C(h(t))(V - V_S). \quad (1)$$

Here,  $C(h)$  is the capacitance, and  $h(t)$  is the time-varying height of the probe above the sample. By differentiating Eq. 1 with respect to time, setting equal to zero, and defining for  $V_m \equiv V$  in this condition, we find

$$0 = \frac{dQ}{dt} = \frac{dh}{dt} \frac{dC}{dh} (V_m - V_S). \quad (2)$$

Hence, for finite derivatives  $dh/dt$  and  $dC/dh$ , we see that this condition is satisfied when

$$V_m(x) = V_S(x). \quad (3)$$

In other words, the simplest interpretation of raw SKPM data is that it is an exact, point-by-point copy of the surface potential of interest.

The above analysis doesn't account for the finite size of the probe or long-range electrostatic interactions. These contributions can be incorporated by replacing the simple capacitance,  $C(h)$ , with an integral over a distributed capacitance,  $\mathcal{C}(h, x)$ <sup>13,14</sup>. In this case, the SKPM condition becomes

$$0 = \frac{d}{dh} \int_S (V_m(x) - V_S(\xi - x)) \mathcal{C}(h, \xi) d\xi, \quad (4)$$

where  $\xi$  is an integration variable. Solving this expression for  $V_m$  gives

$$V_m(x) = \int_S P(x, \xi) V_S(\xi) d\xi \quad (5)$$

where we define the PSF,  $P(x, \xi)$ , which accounts for the terms involving the interaction of the probe at location  $x$  with different sample positions  $\xi$ . Hence, a slightly more sophisticated analysis reveals that a raw SKPM measurement is the convolution of the underlying signal with a point spread function corresponding to the finite size of the probe and long-range interactions. It is important to note that the PSF is not unique for a particular probe. Instead, it depends on the sample-probe interaction through the distributed capacitance. For example, this may give rise to completely different PSFs for purely metallic, purely insulating, or mixed insulator-metal samples due to how the probe interacts with the surface or the bulk of the material<sup>19</sup>.

In practice, the situation is more complicated still, though for less obvious reasons. The measured signal depends not only on the electrostatic interactions between the probe and the sample, but also on the feedback system that measures the current and applies the voltage,  $V$ . Both the PID and lock-in amplifier require finite response times to produce stable signals. If the probe travels a significant distance over these timescales, then information from a range of locations is incorporated into the measurement. Additionally, faster scan speeds can introduce additional mechanical noise which will

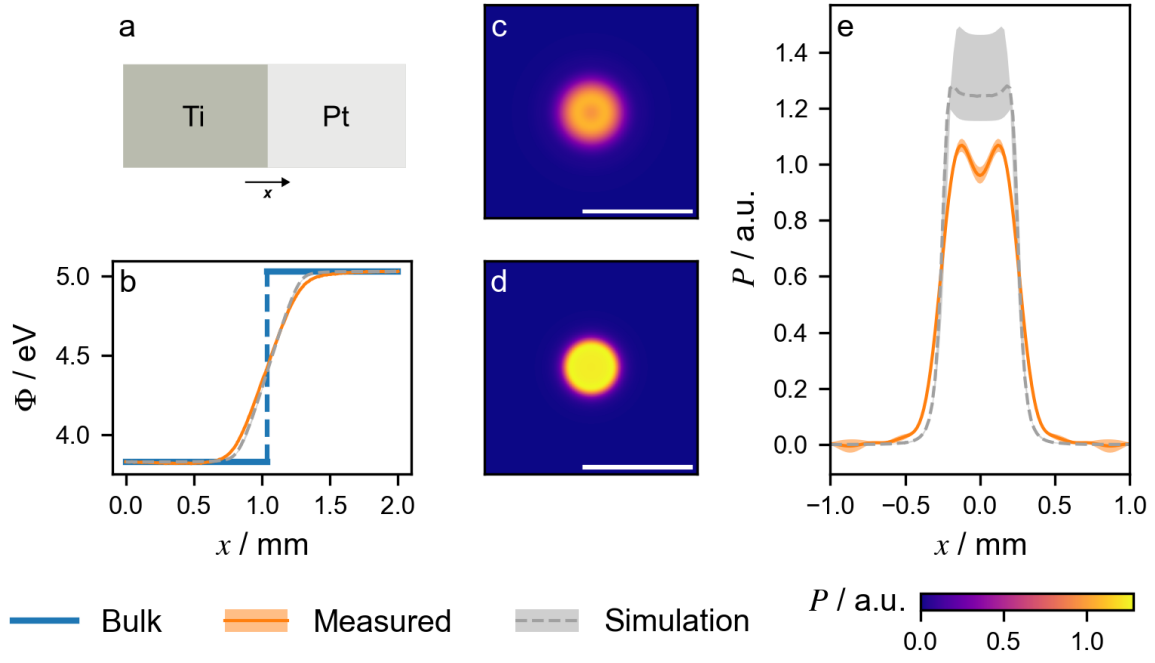


FIG. 2. **Comparison between a PSF estimated using an edge measurement and a simulated PSF.** **a** Scanning an edge created at the boundary between two metals with distinct work functions produces **b** an estimate for the system edge spread function (ESF) along the scan direction. **c** Shows the system PSF estimated from the ESF measurement by assuming that the probe is rotationally symmetric. **d,e** Simulations produce a PSF with a similar width and qualitatively similar shape, but show non-negligible differences, even for a range of different probe geometries (indicated by the shaded region around the simulation line). Scale bars show 1 mm. Shaded regions on measured data represents errors estimated from standard deviation of 9 scans, full details in SM.

further distort the measured signal. Only for a stable system and when the probe is held at each location for long time relative to the response times of the PID/lock-in do we recover Eq. 5. Assuming these processes are linear, we can still write the measured voltage as a purely spatial convolution over a point spread function, but one that is velocity dependent; in other words,

$$V_m(x) = \int P(v|x, \xi) V_S(\xi) d\xi. \quad (6)$$

As the scan velocity approaches zero,  $P(v|x, \xi) \rightarrow P(x, \xi)$ , and the “fast scan” regime (Eq. 6) becomes equivalent to the “slow scan” regime (Eq. 5).

## B. Signal deconvolution

In the previous section, we discussed the forward problem: given an underlying surface potential,  $V_S(x)$ , determine the resulting measurement,  $V_m(x)$ . However, what is usually required is the solution to the inverse problem: given the measurement,  $V_m(x)$ , determine the underlying signal,  $V_S(x)$  (*i.e.*, recover Fig. 1c from Fig. 1b). We start by writing the convolution over the PSF more compactly as

$$V_m = V_S \otimes P. \quad (7)$$

We would like to find an estimate for the true surface voltage map,  $\bar{V}_S$ . In the absence of measurement noise, and for a non-

vanishing  $P$ , we can exactly recover the true surface voltage map,  $V_S$ , by

$$\bar{V}_S = V_m \otimes P^{-1} = (V_S \otimes P) \otimes P^{-1} = V_S, \quad (8)$$

where  $\otimes P^{-1}$  denotes the deconvolution with respect to  $P$ . This expression is relatively easy to calculate by taking advantage of the convolution theorem, *i.e.*

$$\bar{V}_S = \mathcal{F}^{-1} \left( \frac{\mathcal{F}(V_m)}{\mathcal{F}(P)} \right), \quad (9)$$

where  $\mathcal{F}$  and  $\mathcal{F}^{-1}$  represent the Fourier transform and inverse Fourier transform, respectively.

Real systems suffer from measurement noise, which renders the equivalence of  $\bar{V}_S$  and  $V_S$  in Eq. 8 unattainable in practice. Mathematically, independent sources of noise,  $N$ , enter into the equation as  $V_m = V_S \otimes P + N$ , and contain high-frequency components which deconvolution can amplify. To reduce the effect of this, one approach is to simply apply a low-pass filter to  $V_m$ , which can be heuristically motivated given the finite size of probes<sup>20</sup>. However, in order to avoid discarding higher frequency information unnecessarily, an alternative is to use a weighted deconvolution, such as a Wiener filter<sup>13,14</sup>. Mathematically, this manifests itself as a modification to Eq. 9:

$$\bar{V}_S = \mathcal{F}^{-1} \left( \frac{\mathcal{F}(V_m)}{\mathcal{F}(P)} \times \left( \frac{|\mathcal{F}(P)|^2}{|\mathcal{F}(P)|^2 + \frac{1}{\text{SNR}(f)}} \right) \right), \quad (10)$$

where,  $\text{SNR}(f)$  is the signal to noise ratio as a function of spatial frequency. The SNR can either be measured (*e.g.*, by calculating the power spectral density of representative samples with known properties), or in certain circumstances assumed in conjunction with a frequency-relationship for the noise (*e.g.* Brownian noise  $1/f^2$ , pink noise  $1/f$ , *etc.*)

### III. TARGET FABRICATION & MEASUREMENT

To experimentally determine the PSFs, we fabricate calibration targets using materials with different work functions. We work with two different types: an edge target, which produces a large signal but only provides information about the PSF in one direction<sup>21,22</sup>; and a disc target, which allows convenient measurement of the full 2-dimensional PSF from a single 2-dimensional scan. We utilise the edge target for measuring the slow scan PSF (Eq. 5) where we assume rotational symmetry of the PSF and are interested in a very accurate low noise estimate for the probe PSF. We use the disc target for estimating the fast scan PSF (Eq. 6) where the PSF is highly non-axisymmetric and our priority is on performing measurements in reasonable amounts of time under practical conditions.

We fabricate both targets using electron beam evaporation to deposit thin layers of different metals; full details are provided in the Supplemental Materials (SM). The edge target consists of a layer of platinum deposited on a titanium coated glass slide. The physical height of the platinum layer is small (12 nm) compared to the sample-tip separation (60  $\mu\text{m}$ ) so that its geometric influence can be ignored. These metals are chosen for their relatively large work function difference, which due to Fermi equalisation leads to a large contact potential difference and correspondingly large SKPM signal ( $\sim 1$  V). The disc target consists of a small, circular (400  $\mu\text{m}$  diameter) gold disc deposited on a silicon wafer, creating a contact potential difference on the order of 0.5 eV. As with the edge target, the height of the gold-titanium disc is small (103 nm) compared to the scan height. Optical microscopy images of the disc calibration targets are included in the SM.

We perform SKPM measurements using a commercially available device (Biologic, M470). This instrument uses a piezo to oscillate the probe, we use an oscillation frequency of 80 Hz as we notice higher frequencies increase acoustic noise. The oscillation frequency sets of limit on the measurement bandwidth and the achievable resolution at higher scan speeds, as we discuss further in section IV B. We use a closed-loop type SKPM measurement, where a PID feedback controller attempts to minimise the current in the probe. The choice of feedback parameters are important to achieving the best possible bandwidth: too slow a response rate will lead to a broader PSF, while overly aggressive settings can lead to spurious oscillations in the measured signal. Briefly, we use the Ziegler-Nichols method<sup>23</sup> to choose initial guesses for the feedback settings and then make minor adjustments to optimise the results (further details provided in SM).

When SKPM is used for work function measurements, the signal ( $\Delta\Phi$ ) is a relative measurement of the difference in

work function between the probe and sample. To convert Kelvin probe voltages to absolute work function values we use a reference sample of highly ordered pyrolytic graphite (HOPG)<sup>24,25</sup>, additional details are given in the SM. The work function is then given by  $\Phi = \Delta\Phi + \Delta\Phi_{\text{HOPG}}$ , where  $\Delta\Phi_{\text{HOPG}}$  is the difference between the literature value for the HOPG work function and the measured value. To estimate the SNR for deconvolution (*i.e.*, Eq. 10), we look at the power spectral density of a relatively flat region and use this to estimate a power-law relationship between SNR and frequency.

To demonstrate the effect of acquisition parameters and the temporal dependence of acquired measurements, we perform slow scans with step-mode acquisition and fast scans with sweep-mode acquisition. The step-mode acquisition entails moving the probe between specific points and holding it fixed until the SKPM signal has stabilised (*i.e.*, until we can ignore effects from the movement and settling time of the PID/lock-in amplifier). Sweep-mode acquisition involves moving the probe continuously across the sample at a constant velocity, resulting in a temporally distorted signal depending on the scan speed and feedback parameters.

### IV. RESULTS & DISCUSSION

#### A. Experimentally determining PSFs in the quasi-static limit

We now demonstrate how a PSF can be determined experimentally. We start in the slow scan regime, *i.e.* at speeds that are small enough such that Eq. 5 applies. The main difficulty in measuring the slow scan PSF is signal strength compared to measurement noise. Signal strength can be improved by increasing the work function difference between the target and surface or increasing the size of the target, while noise can be reduced with repeated measurements and reduced scan speed. We have found that a good solution for the slow-scan regime is to perform a 1-dimensional scan over a sharp edge between two materials with distinct work functions (Figure 2a). Sharp edges are a common technique for estimating the accuracy and resolution of both SKPM and KPFM systems<sup>26–28</sup>, and they can provide enough information to estimate the PSF for a large cylindrical probe. Even so, extremely slow speeds are required for probe motion to be completely negligible. We utilize a step size of 5  $\mu\text{m}$ , moving at 5  $\mu\text{m/s}$  between points and dwelling at each point for 3.5 s. To improve SNR, we repeat and average multiple lines. In this process, a *single* line scan takes approximately 45 minutes, and the ensemble takes more than seven hours. The final result is shown in Fig. 2b.

To obtain the PSF, we first average multiple scans of the edge to produce a low noise estimate for the edge spread function (ESF). We then calculate the line spread function (LSF) from the derivative of the line scan:

$$\text{LSF}(x) = \frac{d}{dx} \text{ESF}(x). \quad (11)$$

In Fourier space we interpolate the 1-dimensional transform of the line spread function to a 2-dimensional map assuming rotational symmetry and take the inverse Fourier transform to

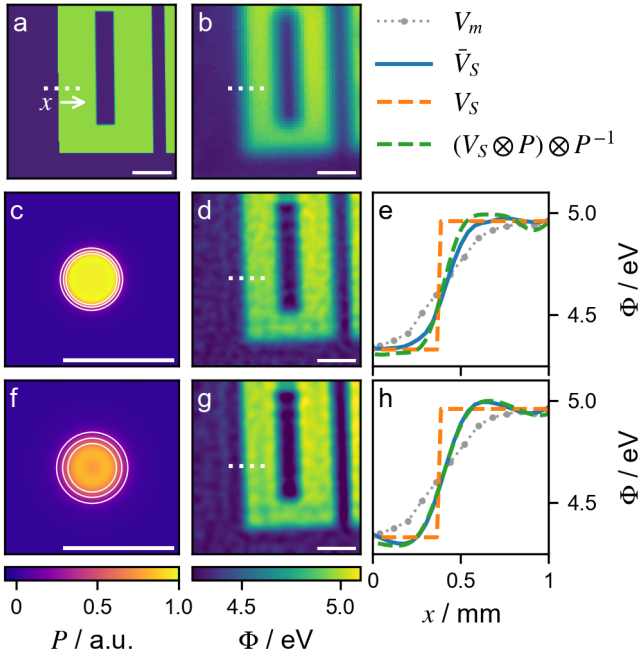


FIG. 3. **Comparison between deconvolution with different PSFs in slow scans.** **a** Scanning a gold-on-silicon target ( $V_S$ ) with sharp features produces **b** a measured ( $V_m$ ) signal with low contrast and blurred-out features. **c–e** Deconvolution with **c** the simulated PSF from Fig. 2d produces **d** an image with higher contrast; however, as shown in **e**, a slice through the deconvolved image ( $\tilde{V}_S$ ) differs from the ideal scenario ( $(V_S \otimes P) \otimes P^{-1}$ ). **f–h** The experimentally measured probe PSF produces a improved estimate for the original signal. Scale bars show 1 mm.

give the PSF. Equivalently, we solve

$$\mathcal{F}_{2D}[\text{PSF}](k_i, k_j) = \mathcal{F}_{1D}[\text{LSF}] \left( \sqrt{k_i^2 + k_j^2} \right)$$

for the PSF, where  $\mathcal{F}_{1D}$  and  $\mathcal{F}_{2D}$  denote the 1-D and 2-D Fourier transforms, and  $k_i, k_j$  are the Fourier space coordinates (see SM for full details). The result is shown in (Fig. 2c). The cross section of this PSF (Fig. 2e) has a non-intuitive feature: a ring of higher intensity towards the edge of the probe. To investigate this further and perform a sanity-check of our strategy, we perform numerical simulations for a second, independent estimate of the PSF (Fig. 2d,e; see SM for details on simulations). In addition, the PSF also has an apparent negative region at around  $\pm 0.8$  mm; however, this measurement is not statistically significant.

The simulations produce a decent estimate for the PSF, but the differences are non-negligible. The simulated PSF has a higher amplitude, is slightly narrower, and exhibits a more subdued ring at the edge. We suspect these differences are due to physical features of the probe that the idealised simulation geometry cannot capture. Our first thought was that the difference was related to an incomplete model of the probe geometry. We included the shield in our simulations as a grounded cylinder around the probe; however, this did not account for the broader PSF shape. Visual inspection of the probe reveals it is not perfectly cylindrical and has a rounded edge (see im-

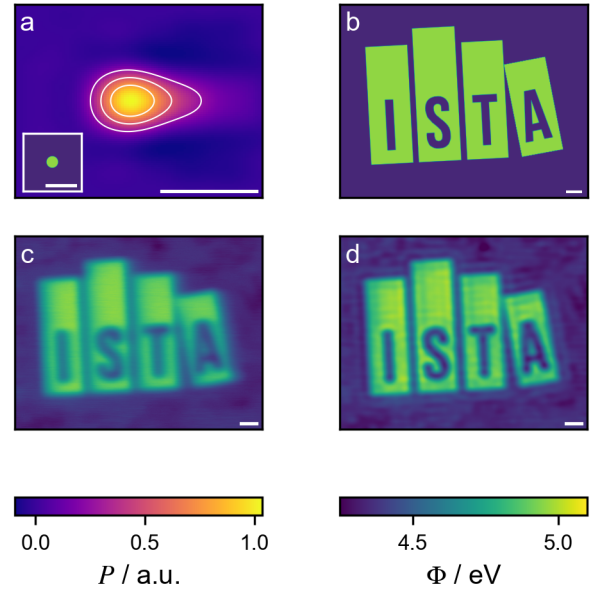


FIG. 4. **PSF and deconvolution for a fast scan.** **a** Fast scans produce a significantly broadened and asymmetric PSF, particularly along the scan direction. **b,c** When the same parameters are used to scan a large target (**b**), this produces a blurred-out image (**c**). **d** Deconvolution of the measured signal with the PSF produces a significantly improved estimate for the underlying signal. Scale bars correspond to 1 mm.

ages in SM). However, simulations exploring a range of edge radii between  $5 \mu\text{m}$  and  $80 \mu\text{m}$  (illustrated by the shaded region in Fig. 2e) show that this alone is not enough to explain the broader PSF width and scale. High-speed video reveals subtle horizontal vibrations in addition to the vertical motion (see SM). A possible explanation for the broader PSF is that these vibrations result in a larger effective probe diameter. The difficulty in constructing an accurate model that fully reproduces the observations even in the slow-scan regime highlights the need for measuring PSFs.

With a PSF in hand, we turn our attention to reconstructing an underlying signal source from an actual measurement. Fig. 3a illustrates our gold-on-silicon target, where the pattern consists a series of vertical/horizontal stripes switching between the two materials. We scan over this target at a slightly lower resolution ( $80 \mu\text{m}$  steps) and slightly larger speed ( $20 \mu\text{m/s}$  with  $0.6$  s dwell time) so that the scan doesn't take unreasonably long. This produces the measured voltage map,  $V_m$ , of Fig. 3b. Using Eq. 10 and the simulated and measured probe PSFs of Fig. 2, we find that we can indeed recover estimates with improved resolution/contrast (Fig. 3c–h). We show in the SM that these recoveries already suffer from slightly elevated scan speed; trying to eliminate temporal information in the PSF entails compromises between speed and resolution that are difficult to balance. As we show in the next section, the better solution is to simply incorporate the probe motion into the PSF.

## B. Determining PSFs for rapid measurements

Without compromising scan speed, we would like to be able to characterise large patterns of interest with high spatial resolution. As mentioned previously, when the distortions introduced by fast scanning are linear, then one can anticipate a velocity-dependent PSF,  $P(v|x, \xi)$ , that nonetheless connects the measured signal,  $V_m$ , to the underlying signal,  $V_S$ , via spatial convolution, as in Eq. 6. In order to acquire this PSF, we straightforwardly perform a scan with the same measurement parameters as we use for the sample measurement. While we could repeat the procedure involving the edge PSF described above, we now no longer have to worry about scanning slowly to stay in a regime where Eq. 5 is applicable. Moreover, scanning fast creates an additional source of broadening to the PSF, making the use of larger targets more practical.

To get a velocity-dependent scan, we now operate the SKPM in sweep (continuous) mode (as opposed to step mode), and with a significantly higher speed of  $200 \mu\text{m/s}$ . To estimate these fast scan PSFs, we explored using 300, 400, and  $500 \mu\text{m}$  diameter discs. Ideally we would want to use a target that is much smaller than the probe diameter; however, we found that the smallest disc produced a signal that was too weak. For  $200 \mu\text{m/s}$  scans, the  $400 \mu\text{m}$  disc was sufficient, but for the faster  $1000 \mu\text{m/s}$  scans we needed to use the  $500 \mu\text{m}$  diameter disc. In order to account for the finite size of the disc, we deconvolved the measured potential by a circular aperture and used a low-pass filter to remove high frequency noise. Full details are provided in the SM.

Figure 4 shows how we put this into practice. Fig. 4a shows the PSF estimated from the scan of the disc shown in the inset. As is visually apparent in the image of the PSF, the velocity dependence blurs the image in the scan direction (left to right). Next, we scan a large and detailed target ( $\sim 1.5 \times 1.0 \text{ cm}^2$ ), as shown in Fig. 4b, which again consists of gold patterned onto a silicon wafer. The scan parameters are intentionally set to be the same as in the PSF of Fig. 4a. The resulting raw voltage map is shown in Fig. 4c. Comparing this to the slower scans of Fig. 2, the spatial blurring is much more apparent – this is in part due to the higher scan speed and chosen feedback parameters. Moreover, it is evident that this has the same left-to-right tail as the corresponding PSF. However, upon spatially deconvolving this scan with the corresponding PSF, the blur is reduced (Fig. 4d).

It is clear from these scans that the PSF shape and resulting signal depend on the acquisition speed; however, it is unclear how the observed broadening depends on the probe size, the introduction of additional noise from scanning at high speeds, the feedback system, and the scan velocity. To explore this further, Figure 5 shows line scans of the target at different speeds using two different probes. The feedback system was tuned to give the fastest possible response to a gold-silicon work function step without introducing too much additional noise. At slow speeds, we see that these settings are sufficient to track the signal given by a small probe scanned slowly over the same region. At high speeds, we see a significant variation in estimated work function – there is a significant lag along the scan direction. Upon deconvolving the measured

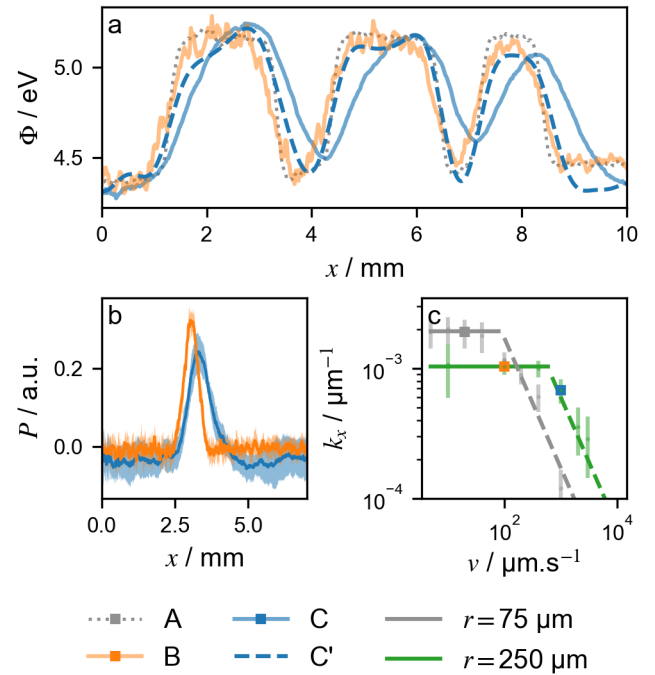


FIG. 5. **Comparison between fast, deconvolved and slow scans.** **a** Partial scan across the target from Fig. 4 using (A) a  $r = 75 \mu\text{m}$  radius probe scanned slowly and averaged over 4 scans, and single scans with a  $r = 250 \mu\text{m}$  radius probe at (B)  $100 \mu\text{m/s}$  and (C)  $1000 \mu\text{m/s}$ . (C') shows the fast scan deconvolved by a PSF estimated from scans of a  $250 \mu\text{m}$  radius disc scanned using the same scan parameters. **b** Scans of the calibration disc with the large probe clearly showing the broadening due to higher scan speed. **c** The effective spatial cut-off frequency,  $k_x$ , estimated for different scan speeds ( $v$ ) with two different probe radii ( $r$ ) using the same scan parameters as in **a**. Squares mark the scans corresponding to the speeds shown in **a**, **b**. Error bars in **b** are estimated from the standard deviation of 10 scans. Error bars in **c** are estimated from the spatial frequency when the signal drops below 10% in frequency space.

signal by a PSF measured at the same speed, we see qualitatively that we recover a significantly improved estimate for the potential. This is very apparent in a line scan across a  $500 \mu\text{m}$  diameter disc (Fig. 5b), where we see the slow scan produces a scan resembling the convolution of two similarly sized circular apertures, while the fast scan produces a reduced signal with a wider distribution.

Unlike in the quasi-static case, the broadening behaviour here is dominated by how quickly the feedback system can respond to a change in the surface work function. Effectively, the highest resolvable spatial frequency in the scan direction is given by

$$k_x = \min \left[ k_{\text{probe}}, \frac{\omega}{v} \right], \quad (12)$$

where  $v$  is the scan velocity,  $k_{\text{probe}}$  is the spatial resolution limited by the probe geometry, and  $\omega$  describes the measurement cut-off frequency. The measurement cut-off frequency depends on both the response rate of the system (i.e., the SKPM oscillation frequency and PID update rate) as well as the cho-

sen feedback parameters, which in turn depend on the signal-to-noise ratio. As a first order approximation, the SKPM signal scales with the probe cross-sectional area; while the noise (ignoring the effects of measurement noise) scales with the square-root of the current signal. This results in a effective bandwidth of

$$\omega \propto \Delta_V r^2 \quad (13)$$

where  $\Delta_V$  is the minimum detectable signal. This trend is illustrated by Fig. 5c, which shows the  $1/v$  fall-off at higher scan speeds and the probe size dependence in the corner frequency (additional measurements showing the noise at different velocities are included in SM). In practice, the cut-off frequency will be lower for a poorly optimised PID and other sources of noise may be dominate at different scan speeds or probe sizes.

## V. CONCLUSION

In this work we demonstrate how the PSFs relevant to scanning Kelvin probe microscopy (SKPM) can be experimentally determined. We find that measured PSFs can differ significantly from those estimated using simulations, especially for rapid scans where the finite response of the feedback system and additional noise further broaden the PSFs. We demonstrate that a practical approach for accounting for the effect of noise in a scan is to measure the PSF using similar scan parameters to those used during measurement acquisition. We utilize two methods for estimating PSFs: one using an edge target, which provides good signal strength but only gives information about the PSF in one direction; and the second using a disc, which provides information about the full 2-dimensional PSF from a single 2-dimensional scan. While both methods could be used to acquire PSFs, we found that the disc was particularly useful for faster scans, where the PSFs tend to be non-axisymmetric. The edge method is more suited to acquiring lower noise PSFs but requires assumptions about the PSF symmetry or multiple measurements with different edge angles to estimate the 2-dimensional PSF.

Our focus has been on characterising the relatively large probes used in SKPM, however, the same procedure could be applicable to characterisation of high speed KPFM measurements. While the larger probes used in SKPM allow direct measurement of the PSF, for smaller probes (such as those used in KPFM), the required spot size and the corresponding decrease in the signal to noise ratio makes experimental measurement of such PSFs difficult. We explore targets involving work function differences between metals, however other approaches such as depositing charge spots or creating an artificial potential step<sup>29</sup> could further improve the signal to noise ratio. Although we focused on SKPM, this procedure could also be useful for characterising and correcting for temporal effects in related methods<sup>16</sup>. Additional modelling of the signal acquisition pipeline could also be useful for determining the effective measurement PSFs from simulated PSFs, this could be particularly relevant for smaller probes such as the nano-scale probes used in KPFM. The results presented

here could be useful for scanning larger samples, particularly with larger probes at faster scanning speeds while achieving decent resolution in the reconstructed images.

## SUPPLEMENTARY MATERIAL

A detailed description of the experimental methods, simulations and additional supporting figures can be found in this article's supplementary material.

## ACKNOWLEDGEMENTS

This project has received funding from the European Research Council (ERC) under the European Union's Horizon 2020 research and innovation program (Grant agreement No. 949120). This research was supported by the Scientific Service Units of The Institute of Science and Technology Austria (ISTA) through resources provided by the Miba Machine Shop, Nanofabrication Facility, Scientific Computing Facility, and Lab Support Facility. The authors wish to thank Dmytro Rak and Juan Carlos Sobarzo for letting us use their equipment. The authors wish to thank the contributions of the whole Waitukaitis group for useful discussions and feedback.

## AUTHOR DECLARATIONS

### Conflict of Interest

The authors have no conflicts to disclose.

### CRedit Author Statement

IL: Conceptualization; Formal analysis; Simulation; Investigation; Writing – Original Draft. FP: Investigation; Resources. LS: Resources. SW: Writing – Review & Editing; Supervision; Funding acquisition.

## DATA AVAILABILITY STATEMENT

The data that support the findings of this study are available from the corresponding author upon reasonable request.

## REFERENCES

- W. A. Zisman, "A new method of measuring contact potential differences in metals," *Rev. Sci. Instrum.* **3**, 367–370 (1932).
- P. P. Craig and V. Radeka, "Stress Dependence of Contact Potential: The Kelvin Method," *Rev. Sci. Instrum.* **41**, 258–264 (1970).
- A. Nazarov and D. Thierry, "Application of Scanning Kelvin Probe in the Study of Protective Paints," *Front. Mater.* **6**, 462587 (2019).

- <sup>4</sup>A. Nazarov, M.-G. Olivier, and D. Thierry, “SKP and FT-IR microscopy study of the paint corrosion de-adhesion from the surface of galvanized steel,” *Progress in Organic Coatings* **74**, 356–364 (2012), application of Electrochemical Techniques to Organic Coatings.
- <sup>5</sup>H. T. Baytekin, A. Z. Patashinski, M. Branicki, B. Baytekin, S. Soh, and B. A. Grzybowski, “The Mosaic of Surface Charge in Contact Electrification,” *Science* **333**, 308–312 (2011).
- <sup>6</sup>X. Bai, A. Riet, S. Xu, D. J. Lacks, and H. Wang, “Experimental and Simulation Investigation of the Nanoscale Charge Diffusion Process on a Dielectric Surface: Effects of Relative Humidity,” *J. Phys. Chem. C* **125**, 11677–11686 (2021).
- <sup>7</sup>T. Hackl, G. Schitter, and P. Mesquida, “AC Kelvin Probe Force Microscopy Enables Charge Mapping in Water,” *ACS Nano* **16**, 17982–17990 (2022).
- <sup>8</sup>Ørjan G. Martinsen and A. Heiskanen, “Chapter 7 - electrodes,” in *Bioimpedance and Bioelectricity Basics (Fourth Edition)*, edited by Ørjan G. Martinsen and A. Heiskanen (Academic Press, Oxford, 2023) fourth edition ed., pp. 175–248.
- <sup>9</sup>M. Nonnenmacher, M. P. O’Boyle, and H. K. Wickramasinghe, “Kelvin probe force microscopy,” *Appl. Phys. Lett.* **58**, 2921–2923 (1991).
- <sup>10</sup>T. Glatzel, U. Gysin, and E. Meyer, “Kelvin probe force microscopy for material characterization,” *Microscopy* **71**, i165–i173 (2022).
- <sup>11</sup>W. Melitz, J. Shen, A. C. Kummel, and S. Lee, “Kelvin probe force microscopy and its application,” *Surf. Sci. Rep.* **66**, 1–27 (2011).
- <sup>12</sup>A. Axt, I. M. Hermes, V. W. Bergmann, N. Tausendpfund, and S. A. L. Weber, “Know your full potential: Quantitative Kelvin probe force microscopy on nanoscale electrical devices,” *Beilstein J. Nanotechnol.* **9**, 1809–1819 (2018).
- <sup>13</sup>G. Cohen, E. Halpern, S. U. Nanayakkara, J. M. Luther, C. Held, R. Bennewitz, A. Boag, and Y. Rosenwaks, “Reconstruction of surface potential from Kelvin probe force microscopy images,” *Nanotechnology* **24**, 295702 (2013).
- <sup>14</sup>T. Machleidt, E. Sparrer, D. Kapusi, and K.-H. Franke, “Deconvolution of Kelvin probe force microscopy measurements—methodology and application,” *Meas. Sci. Technol.* **20**, 084017 (2009).
- <sup>15</sup>B. Ren, L. Chen, R. Chen, R. Ji, and Y. Wang, “Noise Reduction of Atomic Force Microscopy Measurement Data for Fitting Verification of Chemical Mechanical Planarization Model,” *Electronics* **12**, 2422 (2023).
- <sup>16</sup>M. Checa, A. S. Fuhr, C. Sun, R. Vasudevan, M. Ziatdinov, I. Ivanov, S. J. Yun, K. Xiao, A. Sehirlioglu, Y. Kim, P. Sharma, K. P. Kelley, N. Domingo, S. Jesse, and L. Collins, “High-speed mapping of surface charge dynamics using sparse scanning Kelvin probe force microscopy,” *Nat. Commun.* **14**, 1–12 (2023).
- <sup>17</sup>D. Ziegler, T. R. Meyer, R. Farnham, C. Brune, A. L. Bertozzi, and P. D. Ashby, “Improved accuracy and speed in scanning probe microscopy by image reconstruction from non-gridded position sensor data,” *Nanotechnology* **24**, 335703 (2013).
- <sup>18</sup>R. W. Cole, T. Jinadasa, and C. M. Brown, “Measuring and interpreting point spread functions to determine confocal microscope resolution and ensure quality control,” *Nat. Protoc.* **6**, 1929–1941 (2011).
- <sup>19</sup>S. Hudlet, M. Saint Jean, B. Roulet, J. Berger, and C. Guthmann, “Electrostatic forces between metallic tip and semiconductor surfaces,” *J. Appl. Phys.* **77**, 3308–3314 (1995).
- <sup>20</sup>F. Pertl, J. C. Sobarzo, L. Shafeek, T. Cramer, and S. Waitukaitis, “Quantifying nanoscale charge density features of contact-charged surfaces with an FEM/KPFM-hybrid approach,” *Phys. Rev. Mater.* **6**, 125605 (2022).
- <sup>21</sup>C. D. Claxton and R. C. Staunton, “Measurement of the point-spread function of a noisy imaging system,” *J. Opt. Soc. Am. A, JOSAA* **25**, 159–170 (2008).
- <sup>22</sup>X. Zhang, T. Kashti, D. Kella, T. Frank, D. Shaked, R. Ulichney, M. Fischer, and J. P. Allebach, “Measuring the modulation transfer function of image capture devices: what do the numbers really mean?” in *Proceedings Volume 8293, Image Quality and System Performance IX*, Vol. 8293 (SPIE, 2012) pp. 64–74.
- <sup>23</sup>J. ZIEGLER and N. NICHOLS, “Optimum settings for automatic controllers,” *Transactions of the ASME* **64**, 759–768 (1942).
- <sup>24</sup>W. N. Hansen and G. J. Hansen, “Standard reference surfaces for work function measurements in air,” *Surf. Sci.* **481**, 172–184 (2001).
- <sup>25</sup>P. A. Fernández Garrillo, B. Grévin, N. Chevalier, and Ł. Borowik, “Calibrated work function mapping by Kelvin probe force microscopy,” *Rev. Sci. Instrum.* **89** (2018), 10.1063/1.5007619.
- <sup>26</sup>H. N. McMurray and G. Williams, “Probe diameter and probe–specimen distance dependence in the lateral resolution of a scanning Kelvin probe,” *J. Appl. Phys.* **91**, 1673–1679 (2002).
- <sup>27</sup>U. Zerweck, C. Loppacher, T. Otto, S. Grafström, and L. M. Eng, “Accuracy and resolution limits of Kelvin probe force microscopy,” *Phys. Rev. B* **71**, 125424 (2005).
- <sup>28</sup>M. Wicinski, W. Burgstaller, and A. W. Hassel, “Lateral resolution in scanning Kelvin probe microscopy,” *Corros. Sci.* **104**, 1–8 (2016).
- <sup>29</sup>M. Brouillard, N. Bercu, U. Zschieschang, O. Simonetti, R. Mittapalli, H. Klauk, and L. Giraudet, “Experimental determination of the lateral resolution of surface electric potential measurements by Kelvin probe force microscopy using biased electrodes separated by a nanoscale gap and application to thin-film transistors,” *Nanoscale Adv.* **4**, 2018–2028 (2022).

# Beyond the blur: using experimentally determined point spread functions to improve scanning Kelvin probe imaging (Supplementary Material)

Isaac C.D. Lenton, Felix Pertl, Lubuna Shafeek, Scott R. Waitukaitis

June 2024

## S1 Comparison between SKPM and KPFM

Although similar, KPFM and SKPM operate based on different principals: SKPM involves measuring the current in a vibrating probe, while KPFM involves measuring the forces acting on a vibrating cantilever. Although subtle, this difference determines the resolution and range where these two instruments are applicable: KPFM is better suited to high resolution small range scans, while SKPM is well suited to large area scans with high speeds. Here we include a brief discussion about the similarities/differences between the two techniques. We note there are many different realisations of the two techniques (for example, open-loop vs closed-loop SKPM) and, while we try to keep the discussion general, the following may not apply to all instruments/techniques.

In both SKPM and KPFM, resolution typically scales with the probe radius. Smaller probes allow for higher resolution scans, but due to their size they may be more sensitive to noise. SKPM measures the current induced in the probe. In typical electrometers/amplifiers, currents as small as 1fA can be detected. This sets a lower limit on the smallest probe size that can be used in SKPM. Commercial instruments typically have probes ranging down to  $\mu\text{m}$  to 10s of  $\mu\text{m}$  in size. In KPFM, the detected signal is related to the force on the cantilever holding the probe, allowing much smaller (i.e., nm to  $\mu\text{m}$  scale) probes.

While both techniques can achieve fairly high line-scan speeds (on the order of  $100 \mu\text{m/s}$ ), area scan speed is directly related to the number of 1-dimensional line scans required to scan a 2-dimensional area. To achieve the same resolution in both the scan direction and the direction perpendicular to the scan direction requires  $l/\lambda$  line scans, where  $\lambda$  is the spatial resolution and  $l$  is the scan length. In other words, it would take a scan using a 1 nm probe 1000 times longer to complete compared to a 1  $\mu\text{m}$  probe. Reducing the number of scan lines when using a high resolution probe will not necessarily result in a decrease in resolution since the probe has a finite bandwidth. Due to the difference in probe size, and the corresponding difference in area scan speed, these techniques are often complementary: KPFM is able to scan small features with high resolution, while SKPM is able to scan very large samples at rapid speeds.

Another important difference is related to the measurement frequency (in SKPM, this is the vibration frequency and in KPFM this is usually related to the resonance frequency of the cantilever). In KPFM, kHz modulation frequencies can be achieved due to the high resonance frequencies of cantilevers. In SKPM, the increased probe size, as well as the shielding and electronics used to measure the current result in more massive systems and typically lower modulation frequencies (Hz-kHz). In both SKPM and KPFM, the time resolution is directly dependent on the detection frequency, which is typically limited by either the detection electronics or the cantilever frequency.

Despite these differences, both KPFM and SKPM are sensitive to both long and short range electrostatic interactions. The measured signal is often broadened due to the finite size of the probe and long-range electrostatic interactions as well as effects of the feedback system and scanning speed. When these effects are linear, they can be characterised by an appropriate point spread function (i.e., Eq. 5 and Eq. 6).

## S2 Experimental Methods

### S2.1 SKPM measurement

For all SKPM measurements we used the Biologic M470 scanning kelvin probe module. Except where otherwise noted, all measurements used a 500  $\mu\text{m}$  diameter probe (U-SKP370/1, Biologic). The sample was mounted on a tip-tilt-rotation stage (TTR001/M, Thorlabs) with a custom sample holder. For most samples, we used 100 mm diameter silicon wafers as these were easy to handle and mount on the stage. The wafers were electrically connected to the SKPM by attaching a piece of copper tape (AT526, Advance Tapes) near the edge of the wafer to more easily allow connecting the M470. To ensure a good electrical connection between the tape and wafer, we scratched the wafer surface with a diamond scribe and used silver paint (123-9911, RS Pro) to electrically connect the scratched region to the tape. We connected the platinum-titanium target using a similar method except the silver paint could be applied directly to the platinum without needing to first scratch the surface. Prior to measurement, samples were levelled by making multiple capacitive height measurements at different locations across the sample and adjusting the stage. The probe was then positioned at the desired height above the sample (60  $\mu\text{m}$  from the surface for figures 2–4, and 80  $\mu\text{m}$  for figure 5). Key scan parameters are given in Table S1.

	Pt-Ti Edge	Course Scan	Fast Scan	Line Scans
Pixel Size ( $\mu\text{m}$ )	5	80 $\times$ 80	20 $\times$ 40	20
Movement Speed ( $\mu\text{m}/\text{s}$ )	5	20	200	20
Scan Mode	Step	Step	Sweep	Step
Acquisition rate (S/s)	8000	8000	–	8000
Acquisition duration (S)	20000	4000	–	12000
Pre-delay (s)	1	0.1	–	0.1

Table S1: Scan parameters used throughout this work for: platinum-titanium (Pt-Ti) Edge (Fig. 2), Course Scan (Fig. 3), Fast Scan (Figure 4), and Line Scans (Figure S5). For step-mode scans, the dwell time is estimated from acquisition duration and pre-delay time.

### S2.2 Work function calibration

We calibrated the SKPM signal by measuring the potential using freshly exfoliated Highly Ordered Pyrolytic Graphite (HOPG, G3389, Agar Scientific). HOPG was freshly exfoliated using tape (Scotch Magic Tape, Scotch Brand). Care was taken to completely remove a whole layer of graphite. After mounting and levelling the sample, the SKPM probe was positioned 100  $\mu\text{m}$  from the HOPG surface and the potential was measured for different system gain parameters. Different SKPM probes can have different calibration factors. Table S2 compares 2 large probes (U-SKP370/1, Biologic) and 1 small (U-SKP-150). We noticed that the voltage offset depends not only on the probe, but also the electrometer gain. The relationship between offset and gain does not appear to be independent of probe, possibly due to the shift in phase required to maximise the signal. To convert the relative SKPM signal to an absolute work function difference, we compare the measured value for HOPG with the literature value of HOPG to give us an estimate for the work function offset  $\Delta\Phi_{\text{HOPG}}$ . This approach gives a reasonably accurate estimate for the absolute work function. However, due to the variability in the literature values for the work function of HOPG and possible variations in experimental conditions, this calibration procedure may not be sufficient for all applications. Alternatives include direct measurement of the sample work function, for instance, using ultraviolet photo-electron spectroscopy. The results presented in this work all used Probe 3 as the large probe, and Probe 2 as the small probe.

### S2.3 Platinum-titanium sample fabrication

To measure the point spread function from an edge (Fig. 2), we created a calibration target with platinum and titanium, since these materials have a large work function difference. A glass slide was cleaned using Acetone (2 minutes ultrasonic bath) and rinsed with isopropanol before baking at 140°C for 2 minutes to remove any residual water. The glass was then cleaned using a plasma cleaner (1 minutes, 0.5 mbar  $\text{O}_2$ , 240 W), and immediately transferred to the electron beam evaporator (HV Plassy, Plassys Bestek) and

	Probe 1	Probe 2	Probe 3
Diameter ( $\mu\text{m}$ )	500	150	500
LIA Phase (deg)	136	131	133
Voltage (V)			
Gain: 1	0.016	-0.183	0.006
Gain: 10	0.022	-0.167	0.124
Gain: 100	0.0140	-0.17	0.065
Gain: 1000	2.67	4.4	2.5
Gain: 10000	0.723	2.2	0.52

Table S2: Measured SKPM voltages against HOPG calibration target for different tip and gain parameters.

pumped to  $5 \times 10^{-7}$  mBar. 3 nm titanium was evaporated at 0.1 nm/s. The chamber was vented and a mask was applied to half of the titanium surface (Kepton tape). The system was pumped again to  $5 \times 10^{-7}$  mBar, 2 nm additional titanium was deposited at 0.1 nm/s and 10 nm Pt at 0.1 nm/s. Measurements using this sample were performed throughout the following week. We noted that the work function values changed significantly over the following months when this sample was reused, we suspect this is due to surface contamination or another deterioration process.

## S2.4 PSF estimation from edge

To estimate the quasi-static PSF, we first calculated the line spread function (LSF) from the measured edge spread function (ESF),

$$\text{LSF}(x) = \frac{d}{dx} \text{ESF}(x).$$

In order to reduce the noise, we averaged multiple scans of the edge and low-pass filtered the result. We took extra care to make sure the edge was aligned perpendicular to the scan direction by first taking multiple scans at different positions along the edge. The mean of each scan was subtracted to account for instrument drift between scans and the uncertainty was estimated from the standard deviation between scans after subtracting the mean. The numerical derivative was then calculated using a 4-point central difference method and the result low-pass filtered to further reduce noise. Errors were propagated through the low-pass and numerical difference steps assuming the measurement uncertainty is significantly larger than the additional uncertainty introduced from the numerical differentiation. To estimate the PSF from the line spread function, we calculated the Fourier transform of the line spread function and interpolated the 1-D Fourier transform radially into 2-D before taking the inverse Fourier transform to give the point spread function. Equivalently, we solve

$$\mathcal{F}_{2D}[\text{PSF}](k_i, k_j) = \mathcal{F}_{1D}[\text{LSF}] \left( \sqrt{k_i^2 + k_j^2} \right)$$

for the PSF, where  $\mathcal{F}_{1D}$  and  $\mathcal{F}_{2D}$  denote the 1-D and 2-D Fourier transforms, and  $k_i, k_j$  are the Fourier space coordinates. Errors were propagated using the same interpolation approach, however, we note that this may underestimate the errors in the final PSF. To compare PSFs, we apply an area normalisation to the 2-D PSF surface.

## S2.5 Gold lift-off lithography sample fabrication

To fabricate the gold-on-silicon samples (used in Fig. 3 & Fig. 4) we used a photolithography procedure, briefly outlined below. New silicon wafers (p-type, Boron,  $\langle 100 \rangle$ , polished) were cleaned in isopropanol for 2 minutes in an ultrasonic bath on high power and then rinsed briefly with additional isopropanol. Wafers were dried using nitrogen, and heated on a hot plate at  $170^\circ\text{C}$  for 2 minutes. An adhesion promoter (VM652 – a solution of  $\alpha$ -amino propyltriethoxysilane in an organic solvent) was spin coated on the wafer to assist in adhesion of the lift-off resist. A layer of LOR5B (Micro resist technology) resist was spin coated on the wafer (2000 rpm for 45 s). The wafers were baked on a hotplate for 5 minutes at  $170^\circ\text{C}$ . Two layers of positive

photoresist (Microposit S1818, Micro resist technology) were then spin coated on top of the lift-off resist (6,000 rpm for 30 s). After each photoresist coating, the wafer was baked for 1 minute at 115°C.

The coated wafers were then UV exposed using a mask aligner (EVG 610, EV Group) with a mercury bulb light source. Patterns for the calibration targets and work function targets were designed using Creo Parametric and printed on 0.18mm Polyethylene terephthalate (PET) film (JD PhotoData). The mask was mounted on a 1.5 mm glass plate to more easily load it into the mask aligner. The wafer and pattern was then loaded into the mask aligner and exposed to 150mJ/cm<sup>2</sup>. Post exposure, the wafer was baked for 1 minute at 115°C.

The pattern was then developed by immersion in a beaker of MF-319 Developer (Micro resist technology) for 40 seconds and then transferred to a beaker with de-ionised water and visually inspected. If the sample needed additional development, the sample was transferred back into the MF-319 beaker for 5 second intervals. The sample was then rinsed in two baths of de-ionised water and dried with nitrogen.

For metal deposition we used an electron beam evaporator (HV Plassy, Plassys Bestek). We first prepared the wafer surface using oxygen plasma cleaning (240 W, 25 sccm O<sub>2</sub>, 1 minute). Immediately following, we transferred the wafer to the evaporator and pumped down to below 10<sup>-6</sup> mBar. To improve adhesion of the gold, we first deposited 3 nm titanium (0.4 nm/s) before depositing 100nm gold (0.6 nm/s). The increased thickness compared to the titanium-platinum target was chosen to improve durability during handling and future reuse of these targets.

For the lift-off step, we heated DMSO (MicroChemicals) to 50°C in an ultrasonic bath. The wafer was placed in the DMSO bath for 6 minutes and ultrasonic on low power until lift-off was complete. Finally the wafer was rinsed in isopropanol and dried with nitrogen.

## S2.6 Low cost silver calibration target

As an alternative to using targets fabricated using lithography, we also briefly explored using conductive silver paint as a lower cost alternative. To make the low cost target we used a metal wire (diameter 800 μm) dipped in conductive silver paint (123-9911, RS Pro). By carefully contacting the end of the wire with the wafer, we were able to create spots between about 200-400 μm (often multiple attempts were required to produce a nice spot). These low cost targets could be useful for integrating onto existing specimens where the lithography technique is unsuitable.

## S2.7 PSF estimation from disc scans

To estimate the PSF for fast scans, we used a 400 μm diameter gold-on-silicon discs created using the gold lift-off procedure described above. The measured PSFs have a lot of high frequency noise which can adversely affect the deconvolution. To reduce the noise, we filter the measured PSF. A brief summary of the filtering procedure is outlined below.

1. *Load data from SKPM output file.*
2. *De-trend data.* While we attempted to level each sample before scanning, there is often a small tilt still remaining. We attempt to remove this tilt by de-trending the data based on the average slope of the edge values.
3. *Calculate fast Fourier transform.* We apply most of the filtering in frequency space. Before calculating the Fourier transform we pad the measurement with zeros to avoid introducing edge artefacts.
4. *Low pass filter.* To remove the bulk of the high frequency noise, we apply a low pass filter. The choice of cut-off frequency was chosen empirically based on the target signal strength, probe diameter, and inspection of the frequency spectrum image.
5. *Target normalisation.* The ideal calibration target should be much smaller than the probe diameter; however, smaller targets result in poorer signal-to-noise ratios. When using larger calibration targets, we get better signal-to-noise ratios but we need to account for the distortion to the PSF shape. To do this, we divide by the expected frequency spectrum of our calibration target (for circular targets, this

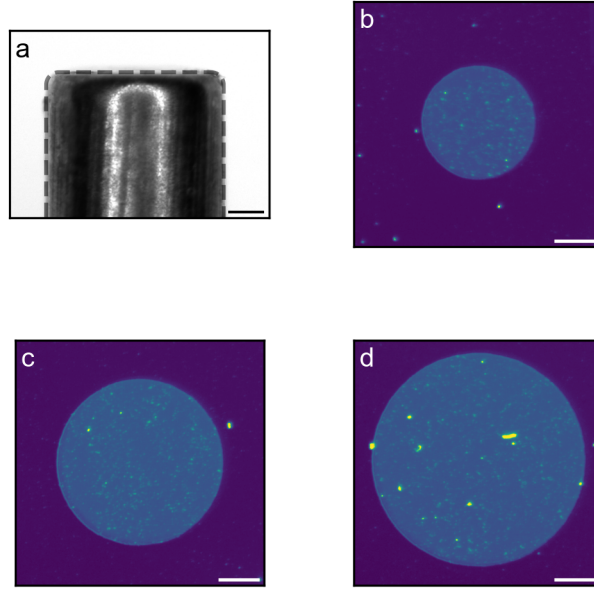


Figure S1: **Optical microscopy images of the probe and calibration targets.** **a** Gray-scale image of the 500  $\mu\text{m}$  probe. The dashed outline shows the profile used for simulations with a 35  $\mu\text{m}$  radius fillet. **b–d** False-colour images of the 300, 400, and 500  $\mu\text{m}$  diameter disc targets. Images were acquired after targets had been used extensively outside the clean room, explaining the accumulation of dust. Scale bars show 100  $\mu\text{m}$ .

is a Jinc function). For calibration targets much smaller than the probe diameter, the frequency space normalisation has little affect since most of the information in frequency space is contained within the central lobe of the Jinc.

6. *Inverse Fourier transform.* We then calculate the inverse Fourier transform to give the filtered PSF. We pad the frequency space image in order to smoothly upsample our PSF (this is important for low-resolution PSFs).
7. *Centring, normalisation and interpolation.* To make it easier to work with our PSF in other routines, we normalise the PSF so the maximum value is 1 (discarding sign), centre the PSF, and create a regular grid interpolator for our PSF. This makes it easier to apply our pre-calculated PSFs to new datasets, regardless of the pixel aspect ratio or resolution.

### S3 Microscopy images of probe and targets

Figure S1 shows optical microscopy images of the circular calibration targets and the 500  $\mu\text{m}$  diameter SKPM probe. While targets were fabricated in our clean room, the SKPM is operated outside the clean room and samples/probes acquire dust/particulate contamination. Compared to the probe diameter, the size of the particulate contamination is typically small and usually only has a minor impact on measurements, even after several months outside our clean room. Before use, we use compressed air to remove large dust from the targets to avoid it potentially coming in contact with the probe.

### S4 COMSOL simulations

To explore the effect of tip geometry on the probe PSF, we built a COMSOL (5.3a) model, shown in Figure S2. The model is mirror symmetric and includes the sample surface, a portion of the probe and

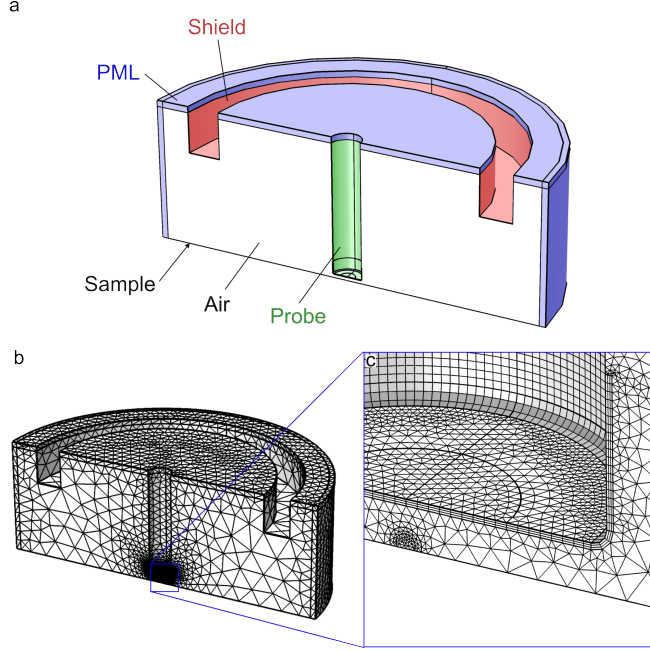


Figure S2: **a** The COMSOL model and **b,c** mesh used for PSF simulations. The model shows the different regions used in the COMSOL simulation including the perfectly matched boundary layer (PML), the conductive layers for the Shield, Probe and Sample, and the air volume being simulated.

Parameter	Value	Parameter	Value
Tip radius	0.25 mm	Shield outer radius	2.79 mm
PML thickness	0.1 mm	Shield inner radius	2.24 mm
Tip height	60 $\mu\text{m}$	Tip displacement	$\pm 15 \mu\text{m}$
Tip rounding	35 $\mu\text{m}$	Target radius	12 $\mu\text{m}$
Far-field radius	3.35 mm	Shield height	1.56 mm
Far-field height	2.34 mm		

Table S3: Key parameters used in COMSOL simulation.

shield, and a surrounding perfectly matched layer (PML). Additional mesh refinement was included around the point defect and around the tip of the probe. The mesh size was chosen in order to produce a smooth surface charge density on the surface and probe. Model parameters are given in Table S3.

To calculate the PSF using this model, we calculated the surface charge on the probe for two different situations: when 1 V was applied to the entire sample; and when 0 V is applied to the sample except for a small disc with non-zero voltage. The probe is positioned at  $a = \pm 15 \mu\text{m}$  from its equilibrium position above the sample. The dimensionless PSF signal is estimated with

$$\text{PSF} \propto \frac{Q(a_+, x) - Q(a_-, x)}{Q(a_+) - Q(a_-)} \quad (1)$$

where  $Q(a_{\pm}, x)$  denotes the surface charge on the tip measured with the disc at position  $x$ , and  $Q(a_{\pm})$  is for a uniform sample potential.

Rounding of the tip has a large effect on the PSF shape. Figure S3a compares tips of the same diameter but with different radius of curvature around the bottom edge of the cylindrical shape. Higher radius of curvature produces a more narrow PSF, but all PSFs still have the same flattop shape with peaks near the edge. Other factors are likely to have a large effect on the PSF shape, for instance, size, uniformity of the probe, oscillation amplitude, and height above the sample. More extensive simulations may produce a improved estimate for the PSF shape.

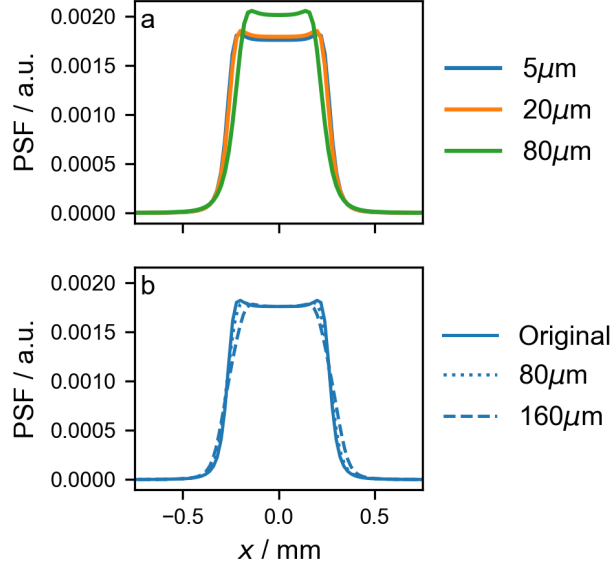


Figure S3: **a** Simulated PSFs with different tip rounding. **b** Low-pass filtered PSFs calculated by convolving a circular aperture with diameters  $80\ \mu\text{m}$  and  $160\ \mu\text{m}$  with the  $5\ \mu\text{m}$  simulated PSF.

To explore the effect of a band-limited measurement of the PSF (such as for too coarse resolution or too high scan speeds), we also looked at low-pass filtering the  $5\ \mu\text{m}$  PSF (Figure 1b). The low-pass filter removes the edge features. This is not the behaviour we see in the experimentally measured PSF in Figure 2e. Instead, this leads us to believe that the difference between the simulated and measured PSFs is related to our model for the tip geometry (the physical probe is not as uniform and visible scratches can be seen in the tip, possibly caused by use or manufacturing defects).

## S5 Fast edge scan PSF estimation

The edge target can also be used for PSF estimation for fast scans as long as the scan is not so fast that the PSF becomes significantly asymmetric. Figure S4 demonstrates how the PSF shape changes when the scan speed is increased from  $5\ \mu\text{m/s}$  to  $100\ \mu\text{m/s}$ . This scan speed still produces a very symmetric PSF, however the PSF is significantly broadened (equivalent to applying a  $800\ \mu\text{m}$  low-pass filter). The broadening means that the effective resolution is much lower, and using a larger calibration target for these higher speed scans (such as a  $400\ \mu\text{m}$  gold disc) should not significantly affect the estimate for the PSF. While there may still be some effect from using a  $400\ \mu\text{m}$  disc as a calibration target, our pre-processing step for fitting the PSF and deconvolving by the disc diameter should reduce the effect in the overall measurement.

## S6 Disc target size

To explore the effect of disc target size on PSF estimation, we also measured different disc with different diameters. The scans are shown in Figure S5. A slightly slower scan speed was used for these scans (helping to resolve the smaller target). All three targets produced a similar shape, although there is still a tiny effect of the target diameter. As expected, the scan of the smaller disc is significantly more noisy. These estimates are all much smaller than the slow measurement PSF shown in Figure S4, suggesting that all the targets are small enough for the fast scan speeds used in Figure 4.

Figure S5 also shows a line scan of a silver calibration target. Although this target is visibly not as circular or uniform as the gold targets, these defects are small compared to the effective measurement PSF, and the results are comparable to the gold targets.

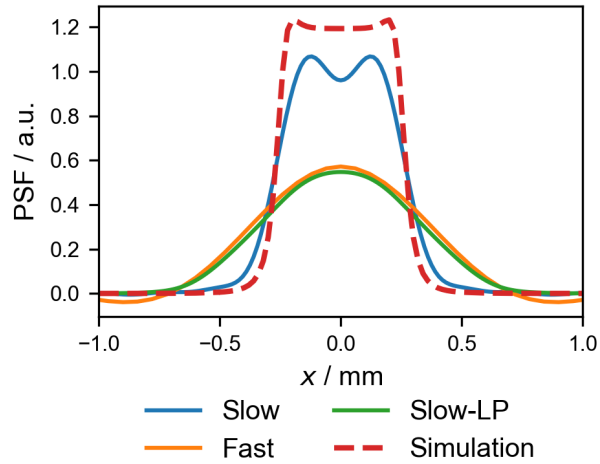


Figure S4: PSFs constructed from an edge scan using a slow ( $5\mu\text{m/s}$ ) and fast ( $100\mu\text{m/s}$ ) scan speeds. The simulation and slow scan correspond to the results presented in Figure 2. Slow-LP shows the fast scan with a  $800\mu\text{m}$  low pass filter.

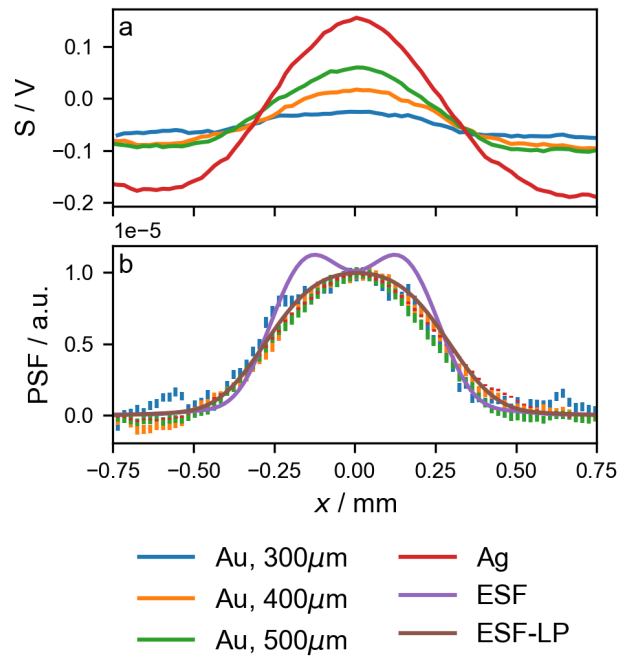


Figure S5: **a** Line scans collected at moderate speeds of gold (Au) and silver (Ag) disc targets. **b** Estimated PSFs using the scans from **a**, with a comparison to the PSF estimated from the ESF and the PSF with a  $300\mu\text{m}$  low-pass filter.

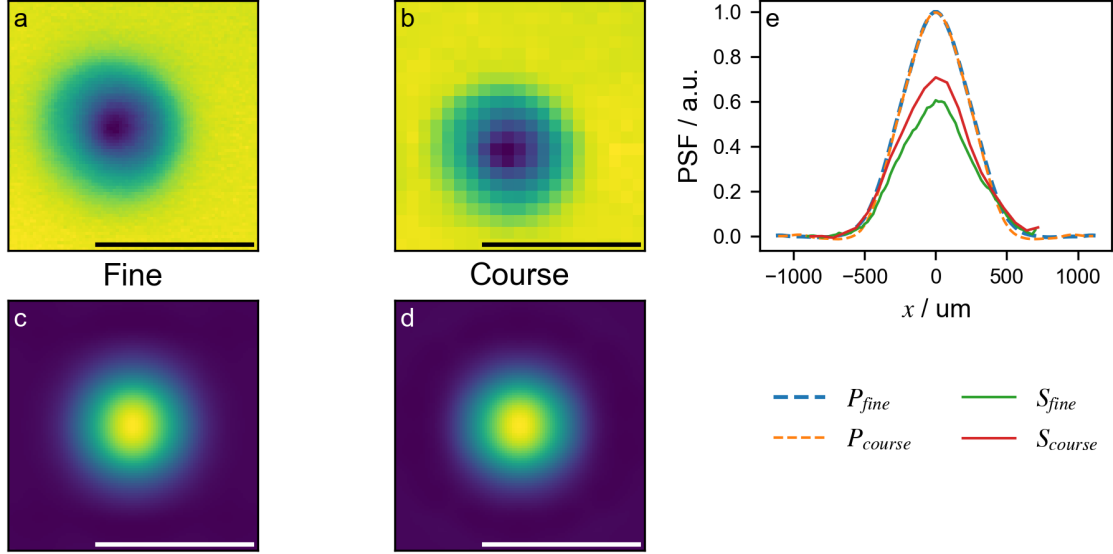


Figure S6: **a,b** Fine and course scans of a small disc-like target. **c,d** Estimated PSFs from the scan. **e** Slices through centre of scans comparing profiles for PSFs,  $P$ , and measured signal,  $S$ .

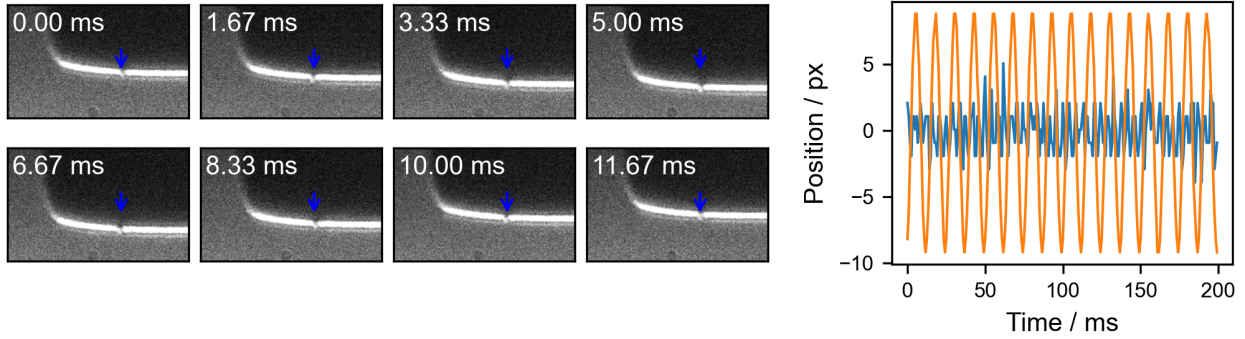


Figure S7: Still images and measured tip trajectory illustrating the motion of the tip. The arrow is meant as a visual guide, indicating a fixed reference spot in each image.

## S7 PSF measurement resolution

Figure S6 compares scan resolution and the estimated PSF shape. While there are some variations between resolution and additional error introduced between the lower resolution scan, the filtering applied for estimating the PSF from these scans seems to produce reasonable/repeatable results.

## S8 Measurement of tip vibration

Using a fast camera (1200 frames per second), we recorded the motion of the SKPM tip. Stills and the estimated trajectory are shown in Figure S7. The tip is vibrated at 80 Hz, and we can clearly see the axial motion of the tip on the camera. We also observe a fair amount of lateral motion, which will likely lead to an effective larger diameter tip. This video was recorded with the probe set to track a fixed position. We expect that the lateral vibrations would increase when the tip is in motion.

## S9 Configuring the instrument for sweep scans

Here we briefly outline the instrument configuration and tuning of the proportional-integral-differential (PID) controller for sweep scans. We find this procedure is suitable for the Biologic M470 SKPM, however it may need some adaptation for other instruments.

1. **Configure probe vibration** These settings largely depend on the chosen probe. We choose settings to avoid acoustic noise. Higher frequencies may increase bandwidth or improve signal-to-noise. The instrument conditioning time should be set to allow any transient vibrations to be damped out before starting the measurement.
2. **Configure movement settings**
  - (a) Choose desired sweep velocity.
  - (b) Set the overscan. The software recommends this be at least 10% of the sweep velocity. Higher values are better as they allow any transient behaviour to be damped out before the measurement acquisition. In practice, this parameter is usually limited by the length of the sample.
  - (c) Set line delay time. This is the time before starting the line scan. This allows the PID controller to stabilise after returning. If a high return velocity is chosen, it may be helpful to increase the line delay time.
  - (d) Set output time constant. This parameter is related to the required voltage resolution and will directly impact achievable measurement resolution/bandwidth in the scan direction.
  - (e) Set analog-to-digital converter sampling rate, PID loop rate and number of samples to average. The manual states that a minimum of about 20 ms is required for the device to perform calculations and respond to communications. The software allows the PID loop rate up to 100Hz (i.e., 10ms), which still seems to produce reasonable results but the instrument seems to take longer to stop when a scan is aborted. This parameter will also limit the effective resolution in fast scans.
3. **Setup acquisition rates**
  - (a) Acquisition rate can be chosen much higher than the PID update rate. Oversampling can help reduce noise in the SKPM voltage measurement, but does not increase resolution. Note: if the (over-)sampling rate is not a factor of the PID update rate, this will result in a different number of points for each sample.
  - (b) Total number of points in scan is limited by micro-controller memory and care should be taken not to exceed it.
  - (c) The system will attempt to adjust the scan distance to a multiple of the step distance – it doesn't always succeed, so its best to check this manually.
4. **Determine PID starting values**
  - (a) It is helpful to do a couple of line scans to determine these values. Do at least two consecutive line scans. If each line scan starts at a different value, you may need to increase the pre-line delay and/or overscan distance.
  - (b) Position the probe above a feature, such as an edge. Set the I and D term to 0. Set a low P value and gradually increase the P value such that a scan from this position causes the signal to decay fast and just begin to oscillate. The oscillations should be smaller than the typical feature height in the scan.
  - (c) There may be multiple oscillation sources, high frequency oscillations are likely from the stepper motors – it may be better to tune the sampling rate to avoid these features.
  - (d) From the critical P value ( $P_c$ ) when oscillations emerge, and the oscillation period ( $\tau$ , in seconds), determine suitable starting values for the I or I/D gains
    - For a P controller: reduce the P value to minimise oscillations. Approximately  $P = 0.5P_c$ .

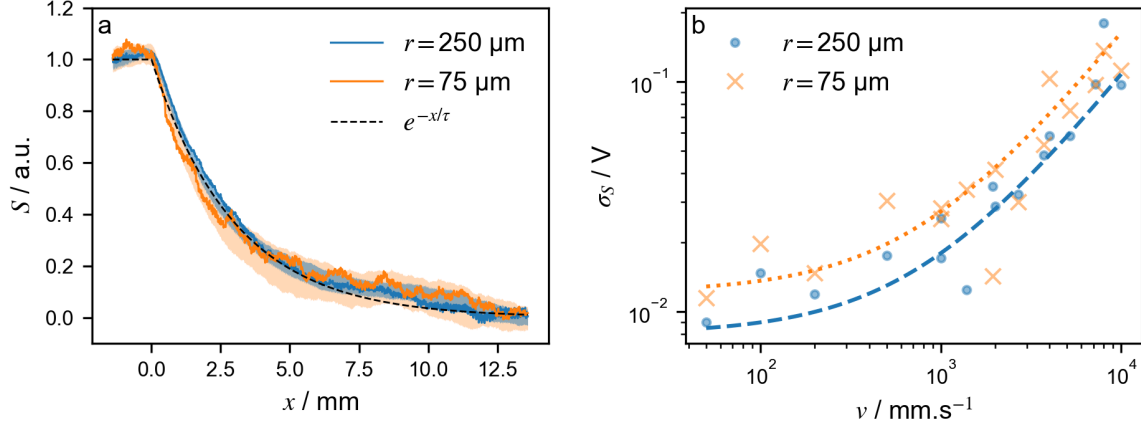


Figure S8: **Effect of noise on large and small probes for comparable response rates.** **a** Smaller probes require higher gain, resulting in an amplification of the noise. Shaded regions show the standard deviation of 10 scans with the corresponding tips. The dashed line shows the exponential decay typical of an over-damped step response. **b** Comparison of the noise as a function of scan velocity for different sized probes. Each point represents the standard deviation of 10 scans. Dashed lines show the expected behaviour.

- For a PI controller:  $P = 0.45P_c$ ,  $I = \frac{1.2P}{G\tau}$ ,
- For PID:  $P = 0.6P_c$ ,  $I = \frac{2P}{G\tau}$ ,  $D = \frac{P\tau}{8G}$ .

where  $G$  is the amplifier gain. At high scan speeds, the derivative term may amplify noise. It may be better to use settings for a PI controller. If significant overshoot is observed, increasing the derivative factor may improve results.

5. **Check performance** It is helpful to check the performance of the PID settings by performing a few line scans and inspecting the results. If necessary, adjust the PID settings.

## S10 Effect of scan speed on noise

For high scan speeds we prefer to use larger diameter probes, since smaller probes do not necessarily result in improved resolution once we consider the increase in noise. This effect can be easily observed by configuring the PID controller so that the system is over-damped and comparing scans of a sharp edge/feature, as shown in Figure S8. In general, we see a larger distribution between measurements with smaller probes. However, at some scan speeds we observe lower variation between scans, possibly due to the shift in stepper motor frequency/noise relative to the SKPM measurement frequency.

## S11 Simulation of large ISTA target

Figure S9 shows a simulation of measurement in Fig. 4 and the deconvolution. The images are qualitatively very similar to the experimental measurements.

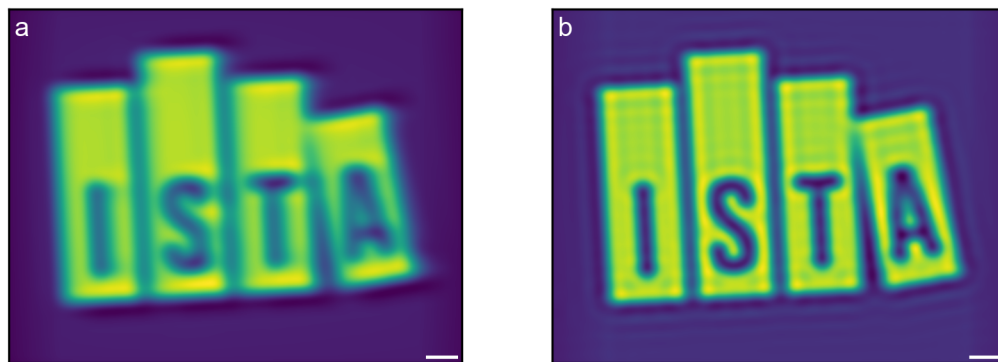


Figure S9: **Simulation of the large ISTA target.** **a** Convolution of the target from Fig. 4a, with the experimentally measured PSF. **b** The recovered estimate for the target after deconvolution. Scale bars show 1 mm.